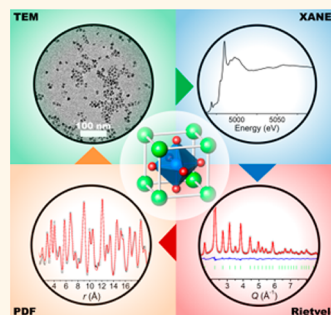


Local Structure of $\text{Ba}_{1-x}\text{Sr}_x\text{TiO}_3$ and $\text{BaTi}_{1-y}\text{Zr}_y\text{O}_3$ Nanocrystals Probed by X-ray Absorption and X-ray Total Scattering

Federico A. Rabuffetti and Richard L. Brutchey*

Department of Chemistry, University of Southern California, Los Angeles, California 90089, United States

ABSTRACT The effect of isovalent chemical substitution on the magnitude and coherence length of local ferroelectric distortions present in sub-20 nm $\text{Ba}_{1-x}\text{Sr}_x\text{TiO}_3$ ($x = 0.0, 0.30, 0.50, 1.0$) and $\text{BaTi}_{1-y}\text{Zr}_y\text{O}_3$ ($y = 0.0, 0.15, 0.50, 1.0$) nanocrystals synthesized at room temperature is investigated using X-ray absorption near edge structure (XANES) and pair distribution function analysis of X-ray total scattering data (PDF). Although the average crystal structure of the nanocrystals is adequately described by a centrosymmetric, cubic $Pm\bar{3}m$ space group, local ferroelectric distortions due to the displacement of the titanium atom from the center of the perovskite lattice are observed for all compositions, except BaZrO_3 . The symmetry of the ferroelectric distortions is adequately described by a tetragonal $P4mm$ space group. The magnitude of the local displacements of the titanium atom in BaTiO_3 nanocrystals is comparable to that observed in single crystals and bulk ceramics, but the coherence length of their ferroelectric coupling is much shorter ($\leq 20 \text{ \AA}$). Substitution of Sr^{2+} for Ba^{2+} and of Zr^{4+} for Ti^{4+} induces a tetragonal-to-cubic transition of the room temperature local crystal structure, analogous to that observed for single crystals and bulk ceramics at similar compositions. This transition is driven by a reduction of the magnitude of the local displacements of the titanium atom and/or of the coherence length of their ferroelectric coupling. Replacing 50% of Ba^{2+} with Sr^{2+} slightly reduces the magnitude of the titanium displacement, but the coherence length is not affected. In contrast, replacing 15% of the ferroelectrically active Ti^{4+} with Zr^{4+} leads to a significant reduction of the coherence length. Deviations from the ideal solid solution behavior are observed in $\text{BaTi}_{1-y}\text{Zr}_y\text{O}_3$ nanocrystals and are attributed to an inhomogeneous distribution of the barium atoms in the nanocrystal. Composition–structure relationships derived for $\text{Ba}_{1-x}\text{Sr}_x\text{TiO}_3$ and $\text{BaTi}_{1-y}\text{Zr}_y\text{O}_3$ nanocrystals demonstrate that the evolution of the room temperature local crystal structure with chemical composition parallels that of single crystals and bulk ceramics, and that chemical control over ferroelectric distortions is possible in the sub-20 nm size range. In addition, the potential of PDF analysis of total scattering data to probe compositional fluctuations in nanocrystals is demonstrated.



KEYWORDS: vapor diffusion Sol–Gel · perovskite · nanoparticles · XANES · total scattering

Perovskite solid solutions $\text{Ba}_{1-x}\text{Sr}_x\text{TiO}_3$ and $\text{BaTi}_{1-y}\text{Zr}_y\text{O}_3$ span a broad range of dielectric phenomena that make them functional materials in complex oxide-based microelectronics. The end members of these solid solutions are BaTiO_3 , SrTiO_3 , and BaZrO_3 . Although they share an ABO_3 perovskite crystal structure consisting of AO_{12} cuboctahedra ($A = \text{Ba}, \text{Sr}$) and BO_6 octahedra ($B = \text{Ti}, \text{Zr}$) as a common feature, their phase diagrams and dielectric behavior differ significantly. BaTiO_3 undergoes three structural phase transitions: rhombohedral ($R3m$) to orthorhombic ($Amm2$) at 183 K, orthorhombic to tetragonal ($P4mm$) at 278 K, and tetragonal to cubic ($Pm\bar{3}m$) at

393 K.¹ The three low temperature phases are ferroelectric, whereas the high temperature phase is paraelectric. SrTiO_3 is a quantum paraelectric featuring a tetragonal ($I4/mcm$) to cubic ($Pm\bar{3}m$) phase transition at 105 K.² The stabilization of the paraelectric state in the low temperature phase is due to zero-point quantum fluctuations of the atomic positions.³ Finally, BaZrO_3 remains cubic ($Pm\bar{3}m$) and paraelectric at all temperatures.

The crystal structure and dielectric properties of ABO_3 perovskites can be rationally tuned through isovalent chemical substitution in the A or B sites. For example, the room temperature crystal structure of

* Address correspondence to brutchey@usc.edu.

Received for review October 28, 2013 and accepted November 26, 2013.

Published online November 26, 2013
10.1021/nn405629e

© 2013 American Chemical Society

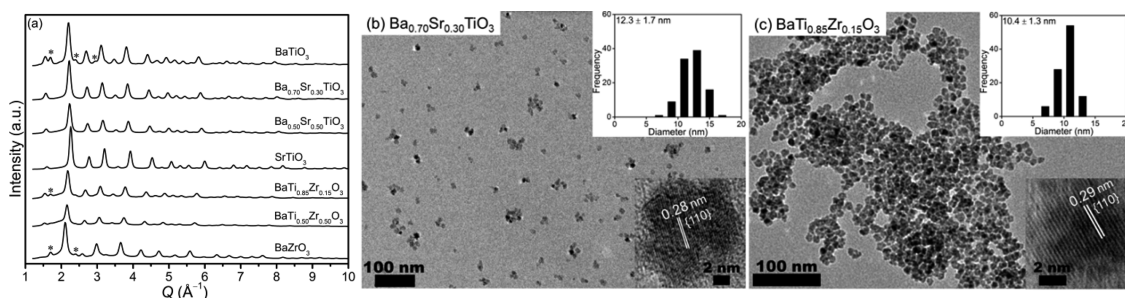


Figure 1. (a) XRD patterns of $\text{Ba}_{1-x}\text{Sr}_x\text{TiO}_3$ and $\text{BaTi}_{1-y}\text{Zr}_y\text{O}_3$ nanocrystals. Diffraction maxima corresponding to BaCO_3 are denoted with the asterisk (*) symbol. TEM images of (b) $\text{Ba}_{0.70}\text{Sr}_{0.30}\text{TiO}_3$ and (c) $\text{BaTi}_{0.85}\text{Zr}_{0.15}\text{O}_3$ nanocrystals. Size distribution histograms obtained by analyzing 100 nanocrystals and high-resolution TEM images of individual nanocrystals are shown in the insets.

$\text{Ba}_{1-x}\text{Sr}_x\text{TiO}_3$ changes from tetragonal to cubic upon substitution of ca. 30–50% of Sr^{2+} for Ba^{2+} .^{4–9} This is accompanied by a decrease in the Curie temperature of the ferroelectric-to-paraelectric transition along with an enhancement of the room temperature dielectric constant.^{5,6} Similarly, $\text{BaTi}_{1-y}\text{Zr}_y\text{O}_3$ has a multiphase point at $y \approx 0.15$ in which rhombohedral, orthorhombic, tetragonal, and cubic phases coexist near room temperature; at this particular substitution level, an enhancement of the room temperature dielectric constant is also observed.^{9–12} This solid solution exhibits normal ferroelectric behavior for $y \leq 0.10$ and relaxor behavior for $0.25 \leq y \leq 0.40$; the ferroelectric-to-relaxor crossover occurs *via* a diffuse phase transition for $0.10 \leq y \leq 0.25$.

Although the phase diagrams of $\text{Ba}_{1-x}\text{Sr}_x\text{TiO}_3$ and $\text{BaTi}_{1-y}\text{Zr}_y\text{O}_3$ solid solutions are well established for single crystals and bulk ceramics, free-standing nanocrystals of these compositions have not been the subject of a systematic composition–structure investigation. Indeed, extensive work has been carried out to understand the structural bases of the “size effect” in ferroelectric BaTiO_3 .^{13–26} Typically, this has been done by probing the atomic arrangement of a set of BaTiO_3 nanocrystals of fixed composition and varying size. However, to the best of our knowledge, no systematic structural studies of perovskite nanocrystals of varying composition and fixed size have been reported. Petkov *et al.*, for example, investigated the crystal structure of 5 nm $\text{Ba}_{1-x}\text{Sr}_x\text{TiO}_3$ nanocrystals ($x = 0, 0.5, 1$), but structural parameters to support the presence (or absence) of local ferroelectric distortions were provided only for BaTiO_3 .²² As a consequence, it remains unclear how the bulk structural picture changes with chemical composition upon reduction of the grain size. Specifically, there is a need to understand how the magnitude and coherence of local ferroelectric distortions change with nanocrystal chemical composition. Indeed, high k nanodielectrics such as $\text{Ba}_{1-x}\text{Sr}_x\text{TiO}_3$ and $\text{BaTi}_{1-y}\text{Zr}_y\text{O}_3$ solid solutions feature polar nanoregions whose dynamics determine the functionality of the nanomaterials.^{9,27–31} Current interest in free-standing perovskite nanocrystals of complex composition arises

from the potential that high k nanodielectrics offer in microelectronics, particularly in terms of device downscaling and integration.³² An area of major interest is the development of solution-based synthetic approaches to the preparation of high-quality thin films showing nanometer-size grains and bulk-like dielectric properties.^{32,33} From this perspective, understanding compositional control of structure–property relations in high k nanodielectrics synthesized using solution-based approaches is of prime importance from both fundamental and applied standpoints.

In this work, X-ray absorption spectroscopy and X-ray total scattering were employed to derive composition–structure relationships for free-standing, sub-20 nm $\text{Ba}_{1-x}\text{Sr}_x\text{TiO}_3$ ($x = 0.0, 0.30, 0.50, 1.0$) and $\text{BaTi}_{1-y}\text{Zr}_y\text{O}_3$ ($y = 0.0, 0.15, 0.50, 1.0$) nanocrystals synthesized at room temperature. Specific chemical compositions were selected to facilitate comparison with phase diagrams derived from structural investigations of single crystals and bulk ceramics. X-ray techniques were chosen to probe the atomic arrangement of the perovskite nanocrystals over complementary length scales. The local atomic environment of the ferroelectrically active Ti^{4+} cation was probed using Ti K edge X-ray absorption near edge structure spectroscopy (XANES). The average and local crystal structure were investigated using Rietveld and pair distribution function (PDF) analysis of X-ray total scattering data. From a structural standpoint, emphasis was placed on elucidating the dependence of the magnitude and coherence of local ferroelectric distortions in $\text{Ba}_{1-x}\text{Sr}_x\text{TiO}_3$ and $\text{BaTi}_{1-y}\text{Zr}_y\text{O}_3$ nanocrystals on chemical composition. From a chemical standpoint, emphasis was placed on assessing the chemical homogeneity of $\text{Ba}_{1-x}\text{Sr}_x\text{TiO}_3$ and $\text{BaTi}_{1-y}\text{Zr}_y\text{O}_3$ nanocrystals, as compositional fluctuations are known to play a crucial role in the dynamics of polar nanoregions.

RESULTS AND DISCUSSION

X-ray diffraction (XRD) patterns and transmission electron microscopy (TEM) images of $\text{Ba}_{1-x}\text{Sr}_x\text{TiO}_3$ and $\text{BaTi}_{1-y}\text{Zr}_y\text{O}_3$ nanocrystals are shown in Figure 1. Diffraction maxima arising from the perovskite phase can

be indexed to the centrosymmetric, cubic $Pm\bar{3}m$ space group. The presence of minor amounts of BaCO_3 (ICSD No. 158378, orthorhombic $Pm\bar{c}n$ space group) is observed in the patterns of BaTiO_3 , $\text{BaTi}_{0.85}\text{Zr}_{0.15}\text{O}_3$, and BaZrO_3 . This carbonate phase results from the chemisorption of atmospheric CO_2 upon postsynthetic exposure of the nanocrystals to air.^{34–36} Nanocrystals belonging to the $\text{Ba}_{1-x}\text{Sr}_x\text{TiO}_3$ solid solution are 8.9 ± 1.5 ($x = 0.0$), 12.3 ± 1.7 ($x = 0.30$), 13.3 ± 2.2 ($x = 0.50$), and 14.8 ± 1.9 ($x = 1.0$) nm in diameter, while those belonging to the $\text{BaTi}_{1-y}\text{Zr}_y\text{O}_3$ solid solution possess diameters of 10.4 ± 1.3 ($y = 0.15$), 11.5 ± 1.5 ($y = 0.50$), and 11.4 ± 1.9 ($y = 1.0$) nm (see Supporting Information). High-resolution TEM images of individual nanocrystals show the presence of well-defined lattice fringes corresponding to the $\{110\}$ crystal planes of the perovskite phase.

X-ray Absorption Near Edge Structure. Ti K edge XANES spectra of BaTiO_3 , $\text{Ba}_{0.70}\text{Sr}_{0.30}\text{TiO}_3$, and $\text{BaTi}_{0.85}\text{Zr}_{0.15}\text{O}_3$ nanocrystals are given in Figure 2. The fine structure of the pre-edge region spanning the 4965–4975 eV energy range provides qualitative and quantitative information about the local atomic environment of the titanium atom.^{37–40} The pre-edge region consists of three peaks centered at ~ 4966.9 (A), 4969.0 (B), and 4972.5 (C) eV. Important in the context of this work is peak B, arising from a Ti $s \rightarrow d-p$ electronic transition;

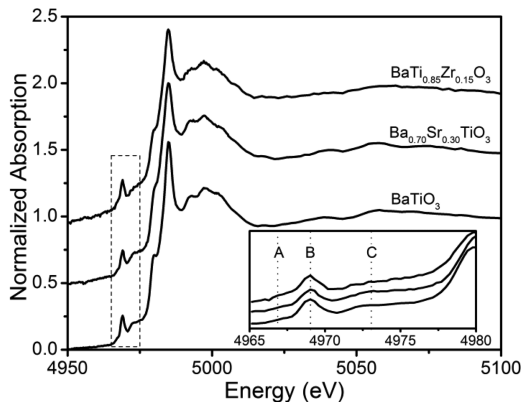


Figure 2. Ti K edge XANES spectra of BaTiO_3 , $\text{Ba}_{0.70}\text{Sr}_{0.30}\text{TiO}_3$, and $\text{BaTi}_{0.85}\text{Zr}_{0.15}\text{O}_3$ nanocrystals. The fine structure of the pre-edge region is shown in the inset.

$d-p$ hybridization occurs due to the displacement of the titanium atom from the instantaneous center of the octahedral oxygen cage. The magnitude of this displacement, defined here as $\Delta_{\text{Ti}-\text{O}_e}$, can be extracted from the area under peak B (see Methods for details). $\Delta_{\text{Ti}-\text{O}_e}$ values of 0.25(1), 0.23(1), and 0.24(1) Å were obtained for BaTiO_3 , $\text{Ba}_{0.70}\text{Sr}_{0.30}\text{TiO}_3$, and $\text{BaTi}_{0.85}\text{Zr}_{0.15}\text{O}_3$, respectively. $\Delta_{\text{Ti}-\text{O}_e}$ in BaTiO_3 nanocrystals is comparable to that reported in previous X-ray absorption investigations of BaTiO_3 single crystals^{38,39} and bulk ceramics.^{38,39,41} This finding gives further support to the notion that the “size effect” in ferroelectric BaTiO_3 does not result from a decrease in the magnitude of local dipoles upon decreasing the grain size, but originates from a reduction in the spatial coherence of their ferroelectric coupling.^{16,20,24} Reduced $\Delta_{\text{Ti}-\text{O}_e}$ values obtained for $\text{Ba}_{0.70}\text{Sr}_{0.30}\text{TiO}_3$ and $\text{BaTi}_{0.85}\text{Zr}_{0.15}\text{O}_3$ nanocrystals indicate that isovalent substitution in the A or B sites reduces the magnitude of the titanium displacement. This reduction is comparable to that reported in previous XANES investigations of chemically substituted BaTiO_3 bulk ceramics.^{41–43}

Rietveld Analysis. Rietveld analysis of XRD patterns was carried out using the cubic $Pm\bar{3}m$ space group. A BaCO_3 phase was included when needed. For this phase, the scale factor and lattice constants were refined. Results from Rietveld analyses are given in Table 1. Fits for two selected compositions are shown in Figure 3 panels a and b; fits for other compositions are given in the Supporting Information. A plot of the cubic lattice constant a as a function of the chemical substitution in $\text{Ba}_{1-x}\text{Sr}_x\text{TiO}_3$ and $\text{BaTi}_{1-y}\text{Zr}_y\text{O}_3$ nanocrystals is shown in Figure 3c. Low R_{wp} values and visual inspection of the fits show that the average (*i.e.*, long-range) crystal structure of $\text{Ba}_{1-x}\text{Sr}_x\text{TiO}_3$ and $\text{BaTi}_{1-y}\text{Zr}_y\text{O}_3$ nanocrystals is adequately described by a cubic unit cell with the titanium atom in the center. The lattice constant of $\text{Ba}_{1-x}\text{Sr}_x\text{TiO}_3$ ($\text{BaTi}_{1-y}\text{Zr}_y\text{O}_3$) nanocrystals decreases (increases) upon increasing x (y), as expected on the basis of ionic radii ($r_{\text{Ba}^{2+}} = 1.42$ Å, $r_{\text{Sr}^{2+}} = 1.26$ Å, $r_{\text{Ti}^{4+}} = 0.61$ Å, $r_{\text{Zr}^{4+}} = 0.72$ Å). In the case of $\text{Ba}_{1-x}\text{Sr}_x\text{TiO}_3$ nanocrystals, a increases linearly with x , indicating an ideal solid solution behavior in which the Ba^{2+} and Sr^{2+} cations are randomly distributed over the A site.

TABLE 1. Rietveld Analysis of X-ray Diffraction Data of $\text{Ba}_{1-x}\text{Sr}_x\text{TiO}_3$ and $\text{BaTi}_{1-y}\text{Zr}_y\text{O}_3$ Nanocrystals

composition	a (Å)	V (Å ³)	U_A (Å ²) ^a	U_B (Å ²) ^a	U_O (Å ²) ^a	BaCO_3 wt % ^b	R_{wp}
BaTiO_3	4.0356(2)	65.725(11)	1.09(6)	1.56(9)	0.27(13)	9.0(2)	3.0
$\text{Ba}_{0.70}\text{Sr}_{0.30}\text{TiO}_3$	3.9998(2)	63.990(9)	1.09(6)	1.55(8)	0.53(11)		2.9
$\text{Ba}_{0.50}\text{Sr}_{0.50}\text{TiO}_3$	3.9785(2)	62.975(11)	1.07(7)	1.59(10)	0.74(14)		2.7
SrTiO_3	3.92056(12)	60.0262(6)	0.85(4)	1.14(5)	0.95(7)		2.4
$\text{BaTi}_{0.85}\text{Zr}_{0.15}\text{O}_3$	4.0716(3)	67.498(16)	1.49(10)	1.61(13)	0.8(2)	3.0(2)	2.7
$\text{BaTi}_{0.50}\text{Zr}_{0.50}\text{O}_3$	4.1117(5)	69.51(2)	1.42(16)	2.7(2)	0.5(3)		3.1
BaZrO_3	4.2107(2)	74.657(13)	1.22(10)	1.25(12)	0.8(2)	12.1(4)	2.3

^a Given as $100 \times U$. ^b Lattice parameters (a , b , c) of BaCO_3 : (a , in BaTiO_3) 5.269(7), 8.967(12), 6.425(8) Å; (b , in $\text{BaTi}_{0.85}\text{Zr}_{0.15}\text{O}_3$) 5.279(15), 8.98(3), 6.418(18) Å; (c , in BaZrO_3) 5.258(9), 8.924(14), 6.445(10) Å.

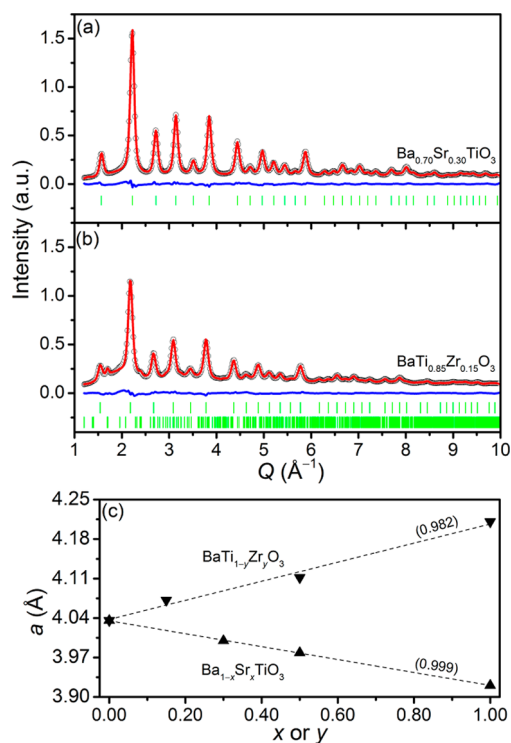


Figure 3. Rietveld analysis of XRD patterns of (a) $\text{Ba}_{0.70}\text{Sr}_{0.30}\text{TiO}_3$, and (b) $\text{BaTi}_{0.85}\text{Zr}_{0.15}\text{O}_3$ nanocrystals. Experimental (\circ) and calculated (red line) patterns are shown along with the difference curve (blue line) and tickmarks (green) corresponding to the phase(s) refined. For $\text{BaTi}_{0.85}\text{Zr}_{0.15}\text{O}_3$, upper and lower tickmarks correspond to the cubic perovskite and orthorhombic BaCO_3 phases, respectively. (c) Evolution of the lattice constant a as function of the chemical substitution. Linear fits to the calculated a values are shown as dashed lines; the corresponding R^2 values are given for each fit.

In contrast, deviations from this ideal behavior are observed for $\text{BaTi}_{1-y}\text{Zr}_y\text{O}_3$ nanocrystals upon substitution of Zr^{4+} for Ti^{4+} in the B site; the origin of these deviations is discussed in detail in the next section.

Despite the ability of the $Pm\bar{3}m$ space group to provide an adequate description of the average crystal structure of perovskite nanocrystals, abnormally low values of the isotropic temperature factor of the oxygen atom (*i.e.*, $U_{\text{O}} < U_{\text{Ti}}$ and $U_{\text{O}} < U_{\text{Ba}}$) were systematically obtained, indicating a deficiency of the cubic structural model. Because XANES spectroscopy provided evidence for the displacement of the titanium atom from the center of the oxygen cage, Rietveld refinements with the noncentrosymmetric, tetragonal $P4mm$ space group were attempted. These, however, yielded unphysical values of the temperature factor of the oxygen atom (*i.e.*, $U_{\text{O}} < 0$), similar to what was observed in earlier structural investigations of sub-10 nm BaTiO_3 nanocrystals.^{22,44} The inability of Rietveld analysis to provide a complete set of reliable structural parameters for the cubic and tetragonal models stems from the reduced structural coherence of the nanocrystals. This intrinsic feature of nanocrystalline materials results in diffuse scattering which, although much

weaker than Bragg scattering,^{45,46} must be taken into account. Structural parameters derived from Rietveld analysis, however, are solely based on the modeling of Bragg scattering.

Pair Distribution Function Analysis. PDF analysis is a total scattering technique that allows both the Bragg and diffuse scattering components of the XRD diffraction pattern to be accounted for when modeling a crystal structure. Experimental PDFs of $\text{Ba}_{1-x}\text{Sr}_x\text{TiO}_3$ and $\text{BaTi}_{1-y}\text{Zr}_y\text{O}_3$ nanocrystals are given in the Supporting Information. Modeling was performed using the cubic $Pm\bar{3}m$ and the tetragonal $P4mm$ space groups. The tetragonal $P4mm$ space group was chosen over the rhombohedral $R3m$ and orthorhombic $Amm2$ space groups on the basis of an earlier structural investigation of 9 nm BaTiO_3 nanocrystals that showed that the tetragonal model provides a better description of the atomic arrangement.⁴⁴ For the $P4mm$ space group, the positions of the oxygen atoms were fixed at $(1/2, 0, 1/2)$ and $(1/2, 1/2, 0)$. Results from PDF analyses are summarized in Table 2. Fits to the experimental PDFs of BaTiO_3 , $\text{Ba}_{0.70}\text{Sr}_{0.30}\text{TiO}_3$, and $\text{BaTi}_{0.85}\text{Zr}_{0.15}\text{O}_3$ in the 1.5–20 Å range are shown in Figure 4, whereas fits for other compositions and in the full interatomic distance range are given in the Supporting Information. The following parameters of the calculated tetragonal models are plotted in Figure 5a–d as a function of the chemical substitution: (1) the average lattice constant $(a^2c)^{1/3}$; (2) the difference between the R_w values obtained for the cubic and tetragonal models defined as: $\Delta R_w = R_w^{Pm\bar{3}m} - R_w^{P4mm}$; (3) the degree of tetragonality of the perovskite unit cell defined as: $t = (c/a - 1) \times 100$; and (4) the mean displacement of the B site cation along the c axis defined as $d_B = z_B \times c$. (Note: d_B values can be considered a good estimate of the average displacement of the titanium atom along the polar axis in $\text{Ba}_{1-x}\text{Sr}_x\text{TiO}_3$ nanocrystals. In the case of $\text{BaTi}_{1-y}\text{Zr}_y\text{O}_3$ nanocrystals, however, d_B values are an estimate of the average displacement of the B site cation (Ti/Zr) along the polar axis, because the local polarization in this solid solution is driven by the displacement of Ti^{4+} cations, while Zr^{4+} cations do not off-center significantly.^{29,31}) For completeness, Figure 5b also includes ΔR_w values for fits performed in the full interatomic distance range.

An inspection of results presented in Table 2 shows that a complete set of physically plausible structural parameters can be extracted from the experimental XRD patterns for both the cubic and tetragonal models. This observation emphasizes the importance of accounting for diffuse scattering when targeting an accurate description of the atomic arrangement in nanocrystals. We note, however, that R_w values and uncertainties of the parameters extracted for $\text{BaTi}_{0.50}\text{Zr}_{0.50}\text{O}_3$ nanocrystals are abnormally high, regardless of the structural model employed. We believe this stems from an unusually low signal-to-noise ratio in the experimental diffraction

TABLE 2. PDF Analysis of X-ray Scattering Data of $\text{Ba}_{1-x}\text{Sr}_x\text{TiO}_3$ and $\text{BaTi}_{1-y}\text{Zr}_y\text{O}_3$ Nanocrystals

composition		a (Å)	c (Å)	z_B	$U_A(\text{Å}^2)^a$	$U_B(\text{Å}^2)^a$	$U_O(\text{Å}^2)^a$	R_w
BaTiO_3	$Pm\bar{3}m$	4.0309(9)		1/2	1.09(6)	2.29(17)	2.8(2)	15.1
	$P4mm$	4.015(2)	4.067(5)	0.467(5)	0.98(8)	1.3(2)	2.7(3)	13.3
$\text{Ba}_{0.70}\text{Sr}_{0.30}\text{TiO}_3$	$Pm\bar{3}m$	3.9953(7)		1/2	1.20(5)	2.22(13)	3.3(2)	14.4
	$P4mm$	3.980(2)	4.031(5)	0.467(4)	1.12(9)	1.2(2)	3.2(3)	12.7
$\text{Ba}_{0.50}\text{Sr}_{0.50}\text{TiO}_3$	$Pm\bar{3}m$	3.9742(9)		1/2	1.26(7)	2.14(16)	3.6(3)	15.3
	$P4mm$	3.958(3)	4.011(6)	0.468(5)	1.19(12)	1.2(3)	3.5(3)	13.7
SrTiO_3	$Pm\bar{3}m$	3.9177(6)		1/2	1.10(6)	1.26(9)	3.30(19)	14.5
	$P4mm$	3.908(3)	3.939(6)	0.481(7)	1.07(13)	0.96(3)	3.2(2)	14.4
$\text{BaTi}_{0.85}\text{Zr}_{0.15}\text{O}_3$	$Pm\bar{3}m$	4.0690(14)		1/2	1.55(12)	2.5(3)	4.0(5)	17.7
	$P4mm$	4.054(5)	4.103(11)	0.469(9)	1.5(2)	1.5(5)	3.9(6)	17.1
$\text{BaTi}_{0.50}\text{Zr}_{0.50}\text{O}_3$	$Pm\bar{3}m$	4.111(2)		1/2	2.1(3)	3.1(5)	5.6(1.1)	22.8
	$P4mm$	4.103(16)	4.13(4)	0.474(19)	2.2(5)	2.3(1.2)	5.4(1.1)	22.5
BaZrO_3	$Pm\bar{3}m$	4.2086(12)		1/2	1.8(4)	1.1(4)	4.8(8)	16.0
	$P4mm$	4.21(5)	4.21(11)	0.50(10)	1.8(4)	1.2(4)	4.8(9)	16.0

^a Given as $100 \times U$.

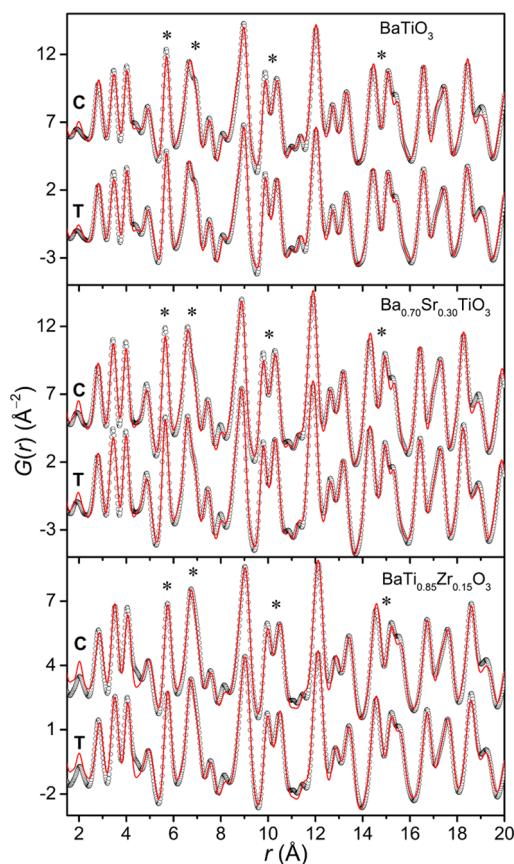


Figure 4. Fits of the cubic (C) and tetragonal (T) models to the experimental PDFs of BaTiO_3 , $\text{Ba}_{0.70}\text{Sr}_{0.30}\text{TiO}_3$, and $\text{BaTi}_{0.85}\text{Zr}_{0.15}\text{O}_3$ nanocrystals in the 1.5–20 Å range. Calculated and experimental PDFs are shown as red solid lines (—) and open symbols (○), respectively. Groups of peaks whose intensity is better described by the tetragonal model are highlighted with the asterisk (*) symbol.

data, likely due to a loose packing of the sample in the Kapton tube. Figure 5a shows that the evolution of the average lattice constant with chemical substitution parallels that extracted from Rietveld analysis. Comparison of residuals of the linear fits to a and $(a^2c)^{1/3}$ values

extracted using Rietveld and PDF analysis, respectively, shows that identical fits are obtained for $\text{Ba}_{1-x}\text{Sr}_x\text{TiO}_3$ nanocrystals. For $\text{BaTi}_{1-y}\text{Zr}_y\text{O}_3$ nanocrystals, in contrast, the quality of the linear fit decreases significantly when the local crystal structure ($R^2 = 0.921$) is considered instead of the average crystal structure ($R^2 = 0.982$). In other words, deviations from Vegard's law, or ideal solid solution behavior, become more significant on a local scale. This suggests chemical inhomogeneity in $\text{BaTi}_{1-y}\text{Zr}_y\text{O}_3$ nanocrystals, which will be discussed in detail in what follows. Figure 5b shows that positive ΔR_w values are obtained for both $\text{Ba}_{1-x}\text{Sr}_x\text{TiO}_3$ and $\text{BaTi}_{1-y}\text{Zr}_y\text{O}_3$ nanocrystals, demonstrating the tetragonal model systematically provides a better fit to the experimental data than the cubic model. The only exception is BaZrO_3 , for which $\Delta R_w = 0.0\%$; therefore, the local atomic arrangement in these nanocrystals systematically deviates from a centrosymmetric cubic structure due to the displacement of the titanium atom from the center of the perovskite lattice. This conclusion is further validated by comparing the results obtained for the cubic and tetragonal models of BaZrO_3 . BaZrO_3 is considered the ideal cubic perovskite, in which the local and average crystal structures are identical.^{47,48} Indeed, the cubic model describes the local crystal structure of BaZrO_3 nanocrystals with equal accuracy as the tetragonal model ($\Delta R_w = 0.0\%$) despite having a smaller number of parameters. Attempts to extract structural parameters for the tetragonal model resulted in abnormally high uncertainties for the lattice constants a and c , indicating overparametrization of the model. This result demonstrates that the systematically better fit provided by the tetragonal model to the experimental PDFs of $\text{Ba}_{1-x}\text{Sr}_x\text{TiO}_3$ and $\text{BaTi}_{1-y}\text{Zr}_y\text{O}_3$ nanocrystals is not an artifact resulting from a larger number of parameters, but reflects the actual presence of polar nanoregions in which the local displacements of the titanium atom are ferroelectrically coupled on a local scale. For a given chemical

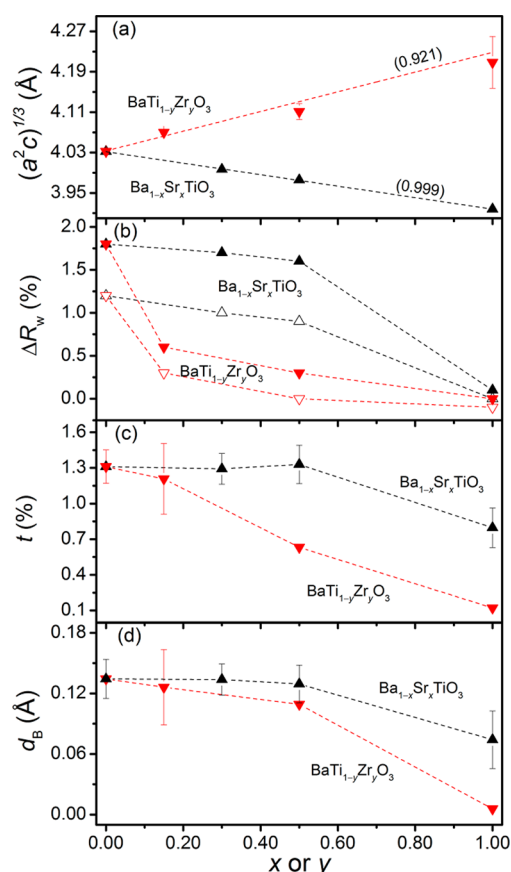


Figure 5. Parameters extracted from the fit of the tetragonal model to the experimental PDFs of $\text{Ba}_{1-x}\text{Sr}_x\text{TiO}_3$ (black \blacktriangle) and $\text{BaTi}_{1-y}\text{Zr}_y\text{O}_3$ (red \blacktriangledown) nanocrystals in the 1.5–20 Å range. (a) Average lattice constant. Linear fits to the calculated values are shown as dashed lines; the corresponding R^2 values are given for each fit. (b) Difference between the R_{wp} values of the fits obtained using the cubic and tetragonal models. ΔR_{wp} values for fits performed in the full interatomic distance range are shown with \triangle and ∇ symbols for $\text{Ba}_{1-x}\text{Sr}_x\text{TiO}_3$ and $\text{BaTi}_{1-y}\text{Zr}_y\text{O}_3$, respectively. (c) Degree of tetragonality of the perovskite unit cell. (d) Mean displacement of the B site cation along the c axis. Error bars for t and d_{B} values of $\text{BaTi}_{0.50}\text{Zr}_{0.50}\text{O}_3$ and BaZrO_3 have been omitted; see text for details. Dashed lines in panels b–d are guides-to-the-eye.

composition, ΔR_{wp} decreases upon extending the fitting range, demonstrating that the ferroelectric coupling between local dipoles progressively loses spatial coherence, thereby making the average crystal structure more cubic-like, in agreement with results from the Rietveld analysis. Likewise, ΔR_{wp} , t (Figure 5c), and d_{B} (Figure 5d) decrease upon increasing x or y , indicating the magnitude of local dipoles and, eventually, their spatial coherence is reduced by chemical substitution (*vide infra*). The extent of this effect is, however, significantly different for $\text{Ba}_{1-x}\text{Sr}_x\text{TiO}_3$ and $\text{BaTi}_{1-y}\text{Zr}_y\text{O}_3$ nanocrystals. Nearly 50% of the Ba^{2+} cations can be replaced with Sr^{2+} with only a slight change in the metrics of the perovskite unit cell and the magnitude of the titanium off-centering. In contrast, replacing the ferroelectrically active Ti^{4+} cation with Zr^{4+} produces a larger effect at substitution levels

as low as 15%. Both compositions observed for these nanocrystals are in agreement with the phase diagrams of $\text{Ba}_{1-x}\text{Sr}_x\text{TiO}_3$ and $\text{BaTi}_{1-y}\text{Zr}_y\text{O}_3$ derived from single crystals and bulk ceramics, which show the critical substitution levels to induce a tetragonal-to-cubic phase transition are $x \approx 0.30$ – 0.50 and $y \approx 0.10$ – 0.20 , respectively. This observation demonstrates the compositional dependence of the crystal structure is not affected by size effects. Dielectric measurements on these nanocrystals have also shown that the dependence of the dielectric constant on chemical composition also parallels that observed in bulk.^{34,35}

Finally, we bring our attention to the case of SrTiO_3 , whose room temperature average crystal structure is described by a cubic $Pm\bar{3}m$ space group. In this work, it is observed that the difference between the fits provided by the cubic and tetragonal models is marginal ($\Delta R_{\text{wp}} = 0.1\%$). However, unlike the case of BaZrO_3 , structural parameters extracted for the tetragonal model exhibit uncertainties that are in line with those observed for the other members of the $\text{Ba}_{1-x}\text{Sr}_x\text{TiO}_3$ solid solution, ruling out overparametrization of the model. In addition, values of t (0.8(2) %) and d_{Ti} (0.07(3) Å) are the smallest observed across the $\text{Ba}_{1-x}\text{Sr}_x\text{TiO}_3$ solid solution, as expected. The presence of polar nano-regions in SrTiO_3 is well-documented in Raman and dielectric studies of bulk ceramics,^{8,49} thin films,⁵⁰ and free-standing 60 nm nanocrystals.⁵¹

Inspection of Figure 4 reveals that the better fit provided by the tetragonal model results from a more accurate description of the intensity of the peak at ~ 5.7 Å and of the doublets at ~ 6.7 and 6.9 , ~ 9.9 and 10.3 , and 14.4 and 15.1 Å. Total PDFs calculated using the cubic and tetragonal models were decomposed into partial PDFs to clarify the origin of this result. Partial PDFs of all the atom–atom pairs present in BaTiO_3 nanocrystals are shown in Figure 6a. Partial PDFs corresponding to B–B pairs (i.e., Ti–Ti, Ti–Zr, and Zr–Zr) present in all other chemical compositions studied in this work are shown in Figure 6b. Figure 6a reveals that the cubic and tetragonal models yield an identical description of the spatial distribution of the all atom–atom pairs in BaTiO_3 nanocrystals. However, PDF peaks arising from Ti–Ti pairs appear sharper in the tetragonal model. Careful inspection of the temperature factors of the B site atom extracted for the cubic and tetragonal models (Table 2) shows the broader B–B peaks observed in the cubic model result from U_{B} values that are artificially enlarged to account for local displacive disorder due to the off-centering of the B atom. This deficiency of the cubic model is relieved in the tetragonal model by allowing the position of the B atom to vary along the c axis. This, in turn, leads to significantly smaller U_{B} values, sharper B–B peaks, and to a better fit to the experimental PDFs. We note that partial Ti–Ti PDFs of the cubic and tetragonal

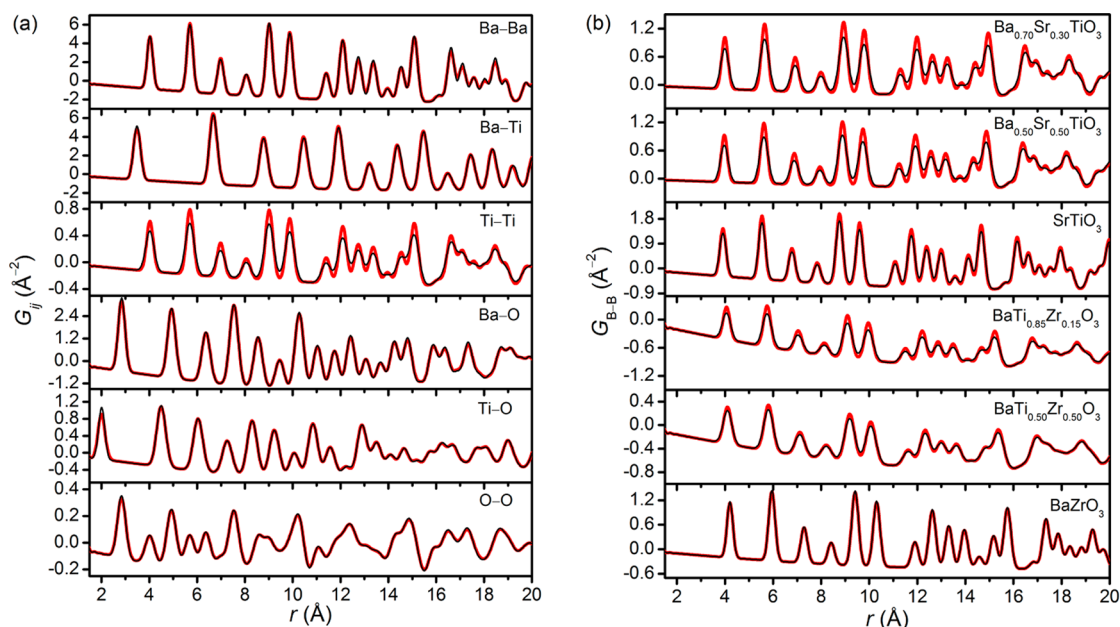


Figure 6. (a) Partial PDFs of BaTiO_3 nanocrystals. (b) B–B partial PDFs of $\text{Ba}_{1-x}\text{Sr}_x\text{TiO}_3$ and $\text{BaTi}_{1-y}\text{Zr}_y\text{O}_3$ nanocrystals. Partial PDFs were computed in the 1.5–20 Å range using the cubic (black line) and tetragonal models (thicker red line).

models of BaTiO_3 differ strongly in the $r \leq 16$ Å range, but become nearly indistinguishable upon approaching 20 Å. Therefore, the coherence length of the ferroelectric coupling between local displacements of the titanium atom along the polar direction can be estimated to be on the order of ~ 16 –20 Å, in good agreement with results reported in earlier structural studies of free-standing BaTiO_3 nanocrystals^{16,22,24} and ultrathin films.⁵² The short coherence length helps to explain the exponential reduction of the dielectric constant of ferroelectric perovskite oxides such as BaTiO_3 upon going from the bulk to the nanoscale.¹⁶ The estimated coherence length does not seem to be significantly affected upon substitution of Sr^{2+} for Ba^{2+} up to levels of 50%. On the basis of this result and the evolution of d_{Ti} (see Figure 5d), it appears that chemical substitution in $\text{Ba}_{1-x}\text{Sr}_x\text{TiO}_3$ nanocrystals leads only to a slight reduction of the magnitude of the local displacement of the titanium atom. In contrast, both the average magnitude of the local displacement d_{B} (Figure 5d) and its coherence length appear to be strongly affected by the substitution of Zr^{4+} for Ti^{4+} in $\text{BaTi}_{1-y}\text{Zr}_y\text{O}_3$ nanocrystals. Indeed, partial B–B PDFs of the cubic and tetragonal models of $\text{BaTi}_{0.85}\text{Zr}_{0.15}\text{O}_3$ and $\text{BaTi}_{0.50}\text{Zr}_{0.50}\text{O}_3$ nanocrystals become nearly indistinguishable at ~ 15 and ~ 12 Å, respectively. These estimates are in good agreement with those in $\text{BaTi}_{1-y}\text{Zr}_y\text{O}_3$ bulk powders reported by Jeong *et al.*⁵³

Finally, we turn our attention to the deviations from the ideal solid solution behavior observed in $\text{BaTi}_{1-y}\text{Zr}_y\text{O}_3$ nanocrystals. Observation of the experimental PDFs for this solid solution reveals an anomalous behavior of the peak located at ~ 2.8 Å, which corresponds to the Ba–O atomic pair. Indeed, the

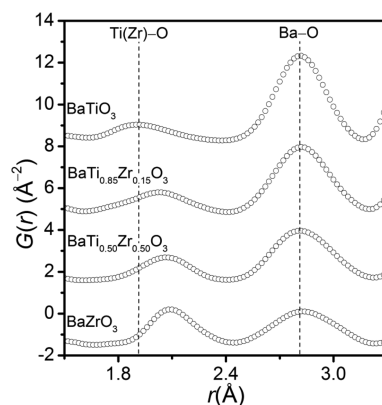


Figure 7. Experimental PDFs (○) of $\text{BaTi}_{1-y}\text{Zr}_y\text{O}_3$ nanocrystals in the 1.5–3.3 Å range; peaks arising from Ti(Zr)–O and Ba–O pairs are indicated.

average Ba–O bond distance remains nearly constant upon an increasing y , while all other interatomic distances increase as expected (Figure 7). In addition, the experimental Ba–O peak broadens upon increasing y , reflecting a broader distribution of Ba–O distances. The fact that the average coordination environment of the barium atom appears increasingly distorted upon increasing the zirconium content indicates an inhomogeneous distribution of the barium atoms, and thus explains the deviations from the ideal solid solution behavior observed in $\text{BaTi}_{1-y}\text{Zr}_y\text{O}_3$ nanocrystals. Such a distribution can result from the presence of barium atoms in the perovskite lattice with a heavily distorted coordination environment.⁵⁴ Alternatively, it can result from the segregation of barium-rich secondary phases whose structural coherence is not large enough to allow detection by Rietveld analysis of X-ray diffraction

data.^{29,55} Therefore, this finding demonstrates the utility of total scattering as a tool to probe compositional fluctuations in nanocrystals synthesized using solution-based approaches and molecular precursors as building blocks.

CONCLUSION

In summary, X-ray absorption and X-ray total scattering were employed to gain fundamental insight into the compositional dependence of polar nanoregions in sub-20 nm $\text{Ba}_{1-x}\text{Sr}_x\text{TiO}_3$ and $\text{BaTi}_{1-y}\text{Zr}_y\text{O}_3$ nanocrystals synthesized at room temperature. The presence of local ferroelectric distortions due to the off-centering of the titanium atom was demonstrated, and their symmetry was adequately described by a tetragonal $P4mm$ space group. Substitution of Sr^{2+} for Ba^{2+} and of Zr^{4+} for Ti^{4+} induced a tetragonal-to-cubic transition of the local crystal structure, analogous to that observed for the average crystal structure of single crystals and bulk ceramics. This structural transition within polar nanoregions was driven by a reduction of the magnitude of the local displacements of the titanium atom and/or of the coherence of their ferroelectric coupling. A reduction of the magnitude of the titanium off-centering was observed upon replacing

50% of Ba^{2+} with Sr^{2+} in $\text{Ba}_{1-x}\text{Sr}_x\text{TiO}_3$ nanocrystals, but the coherence length remained unchanged. In contrast, a noticeable reduction in the coherence length was observed upon replacing 15% of the ferroelectrically active Ti^{4+} with Zr^{4+} in $\text{BaTi}_{1-y}\text{Zr}_y\text{O}_3$ nanocrystals. Results presented in this work show that the evolution of the room temperature local crystal structure with chemical composition mirrors that of single crystals and bulk ceramics, thus suggesting that compositional control over cooperative properties such as ferroelectricity should be possible at the nanoscale, even for nanocrystals as small as 10 nm.

A random distribution of the Ba^{2+} and Sr^{2+} cations over the A site was achieved in $\text{Ba}_{1-x}\text{Sr}_x\text{TiO}_3$ nanocrystals. In contrast, deviations from the ideal solid solution behavior were observed in $\text{BaTi}_{1-y}\text{Zr}_y\text{O}_3$ nanocrystals upon increasing substitution of Zr^{4+} for Ti^{4+} . Analysis of the evolution of experimental PDF peaks' position (bond distance) and width (atomic disorder) pointed to an increasingly inhomogeneous distribution of the barium atoms upon an increase in the zirconium content. This finding highlights the potential of PDF analysis of total scattering data as a tool to investigate compositional fluctuations in nanocrystals synthesized using solution-based approaches and molecular precursors as building blocks.

METHODS

Synthesis of $\text{Ba}_{1-x}\text{Sr}_x\text{TiO}_3$ and $\text{BaTi}_{1-y}\text{Zr}_y\text{O}_3$ Nanocrystals. $\text{Ba}_{1-x}\text{Sr}_x\text{TiO}_3$ ($x = 0.0, 0.30, 0.50, 1.0$) and $\text{BaTi}_{1-y}\text{Zr}_y\text{O}_3$ ($y = 0.0, 0.15, 0.50, 1.0$) nanocrystals were synthesized *via* a vapor diffusion sol-gel method described elsewhere.^{34–36} This method relies on the hydrolysis and polycondensation of a mixture of liquid bimetallic alkoxides (*i.e.*, $\text{BaTi}(\text{OR})_6/\text{SrTi}(\text{OR})_6$ or $\text{BaTi}(\text{OR})_6/\text{BaZr}(\text{OR})_6$, $\text{R} = \text{CH}_2\text{CH}(\text{CH}_3)\text{OCH}_3$) upon slow diffusion of water vapor into the solution. Crystallization of the desired perovskite phase occurs at atmospheric pressure and room temperature, without the need for postsynthetic thermal treatment.

Synchrotron X-ray Diffraction. X-ray diffraction (XRD) patterns were collected at the 11-ID-B line of the Advanced Photon Source at Argonne National Laboratory. An incident photon energy of 90.484 keV ($\lambda = 0.137024 \text{ \AA}$) was employed. Samples were loaded in Kapton tubes and diffraction data were collected in transmission mode at room temperature.

Transmission Electron Microscopy. Transmission electron microscopy (TEM) images were obtained using a JEOL JEM2100F (JEOL Ltd.) electron microscope operating at 200 kV. Samples were dispersed in methanol and deposited on a 200 mesh Cu grid coated with a lacey carbon film (Ted Pella, Inc.). Nanocrystal size distribution histograms were constructed by analyzing 100 individual nanocrystals and assuming spherical shape.

X-ray Absorption Near Edge Structure. X-ray absorption near edge structure (XANES) spectra were collected at the 20-BM-B line of the Advanced Photon Source at Argonne National Laboratory. The incident X-ray beam was monochromatized using a Si(111) double crystal. A harmonic rejection mirror was used to eliminate higher harmonics, and the beam intensity was detuned an additional 10% to further reduce any residual harmonics. Measurements at the Ti K edge (4966 eV) were performed in transmission mode using gas ionization chambers filled with N_2 to monitor the incident and transmitted intensities. Samples were prepared by spreading a thin, uniform layer of powder on Kapton tape. The incident X-ray beam size was $1 \text{ mm} \times 6 \text{ mm}$ (unfocused). XANES spectra were collected at room temperature

under flowing helium. Each spectrum was normalized by subtracting the pre-edge and applying an edge-jump normalization using the Athena software.⁵⁶ The displacement of the titanium atom from the instantaneous center of the octahedral oxygen cage ($\Delta_{\text{Ti-O}_6}$) was derived from the area under peak B (A_B) in the pre-edge region of the XANES spectrum, according to

$$\Delta_{\text{Ti-O}_6} (\text{\AA}) = [(3A_B)/\gamma]^{1/2} \quad (1)$$

where $\gamma = 11.1 \text{ eV \AA}^{-2}$.³⁸ The extraction of A_B was performed by fitting peaks A, B, and C with three Lorentzians; the background was fit in the 4965–4980 eV energy range using a polynomial function.

Rietveld Analysis. Rietveld structural refinements were carried out using the GSAS software.⁵⁷ Experimental data and atomic X-ray scattering factors were corrected for sample absorption and anomalous scattering, respectively. Refinements of the perovskite phase were performed using a mean atom approach, in which substitution in the A or B sites was simulated by changing the occupation factor of the corresponding site and fixing it at the nominal composition. The following parameters were refined: (1) scale factor, (2) background, which was modeled using a shifted Chebyshev polynomial function, (3) peak shape, which was modeled using a modified Thomson–Cox–Hasting pseudo-Voigt function,⁵⁸ (4) lattice constants, (5) fractional atomic coordinates of the B site atom(s) when allowed by symmetry, and (6) an isotropic thermal parameter for each chemical species, regardless of their crystallographic site in the perovskite structure (*i.e.*, U_A , U_B , and U_O). The R_{wp} indicator was employed to assess the quality of the refined structural models.⁵⁹

Pair Distribution Function Analysis. The pair distribution function (PDF) $G(r)$ defined as

$$G(r) = 4\pi r[\rho(r) - \rho_0] = (2/\pi) \int_Q^{Q_{\text{max}}} Q[S(Q) - 1] \sin(Qr) dQ \quad (2)$$

was employed for structural analysis. Here, r is the radial distance, $\rho(r)$ and ρ_0 are the local and average atomic number

density, respectively, and Q is the magnitude of scattering vector defined as

$$Q = (4\pi/\lambda)\sin\theta \quad (3)$$

where 2θ is the angle between incident and scattered X-rays. The RAD software was employed to extract $G(r)$ from the raw diffraction data.⁶⁰ These were first corrected for background, sample absorption, and Compton scattering. Then, normalized structure functions $S(Q)$ were obtained; these are given in the Supporting Information. Finally, $S(Q)$ was Fourier-transformed to yield $G(r)$. For all compositions a maximum scattering vector (Q_{\max}) of 25 \AA^{-1} was employed in the Fourier transform; the two exceptions were $\text{BaTi}_{0.85}\text{Zr}_{0.15}\text{O}_3$ and $\text{BaTi}_{0.50}\text{Zr}_{0.50}\text{O}_3$, for which a maximum scattering vector of 23 \AA^{-1} was used. Structural refinements were carried out using the PDFgui software.⁶¹ Similar to Rietveld analysis, a mean atom approach was employed to simulate chemical substitution. The following parameters were refined: (1) scale factor, (2) lattice constants, (3) fractional atomic coordinates of the B site atom(s) when allowed by symmetry, and (4) an isotropic thermal parameter for each chemical species, regardless of their crystallographic site in the perovskite structure. The R_w indicator was employed to assess the quality of the refined structural models.^{22,45} The calculated total PDF $G(r)$ was decomposed into partial PDFs $G_{ij}(r)$ according to

$$G(r) = \sum_{ij} w_{ij} G_{ij}(r) \quad (4)$$

where the summation runs over all the atomic species contained in the sample, and w_{ij} are the weighting factors defined as

$$w_{ij} = [c_i f_i(Q)] [c_j f_j(Q)] / \sum_i [c_i f_i(Q)]^2 \quad (5)$$

Here, c_i and $f_i(Q)$ are the atomic concentration and X-ray scattering factor of the i th chemical species, respectively, and obey the sums $\sum c_i = 1$ and $\sum w_{ij} = 1$.^{45,62} In this work, $f_i(Q)$ values were corrected for anomalous scattering and evaluated at $Q = 0$.

Conflict of Interest: The authors declare no competing financial interest.

Acknowledgment. This material is based on work supported by the Department of Energy Office of Basic Energy Sciences under Grant No. DE-FG02-11ER46826. The authors thank Dr. Dale Brewre, Dr. Karena Chapman, and Dr. Kevin Beyer from the Advanced Photon Source for their assistance with the collection of X-ray absorption and X-ray scattering data. Dr. Leopoldo Suescun from Cryssmat–Lab/DETEMA, Facultad de Química, Universidad de la República (Uruguay) is also gratefully acknowledged for useful discussions. Use of the Advanced Photon Source at Argonne National Laboratory was supported by the U.S. Department of Energy, Office of Science, Office of Basic Energy Sciences under Contract No. DE-AC02-06CH11357.

Supporting Information Available: (1) Structure functions $S(Q)$; (2) additional TEM images and size distribution histograms; (3) additional Rietveld fits to the experimental XRD patterns; (4) experimental PDFs; (5) additional fits to the experimental PDFs in the 1.5–20 Å range; (6) fits to the experimental PDFs in the full interatomic distance range; (7) calculated partial PDFs. This material is available free of charge via the Internet at <http://pubs.acs.org>.

REFERENCES AND NOTES

- Kwei, G. H.; Lawson, A. C.; Billinge, S. J. L.; Cheong, S.-W. Structures of the Ferroelectric Phases of Barium Titanate. *J. Phys. Chem.* **1993**, *97*, 2368–2377.
- Unoki, H.; Sakudo, T. Electron Spin Resonance of Fe^{3+} in SrTiO_3 with Special Reference to the 110 K Phase Transition. *J. Phys. Soc. Jpn.* **1967**, *23*, 546–522.
- Muller, K. A.; Burkard, H. SrTiO_3 : An Intrinsic Quantum Paraelectric Below 4 K. *Phys. Rev. B* **1979**, *19*, 3593–3602.
- Lemanov, V. V.; Smirnova, E. P.; Szymik, P. P.; Tarakanov, E. A. Phase Transitions and Glasslike Behavior in $\text{Sr}_{1-x}\text{Ba}_x\text{TiO}_3$. *Phys. Rev. B* **1996**, *54*, 3151–3157.
- Zhang, L.; Zhong, W.-L.; Wang, C.-L.; Zhang, P.-L.; Wang, Y.-G. Finite-Size Effects in Ferroelectric Solid Solution $\text{Ba}_x\text{Sr}_{1-x}\text{TiO}_3$. *J. Phys. D: Appl. Phys.* **1999**, *32*, 546–551.
- Zhou, L.; Vilarinho, P. M.; Baptista, J. L. Dependence of the Structural and Dielectric Properties of $\text{Ba}_{1-x}\text{Sr}_x\text{TiO}_3$ Ceramic Solid Solutions on Raw Material Processing. *J. Eur. Ceram. Soc.* **1999**, *19*, 2015–2020.
- Dobal, P. S.; Dixit, A.; Katiyar, R. S.; Garcia, D.; Guo, R.; Bhalla, A. S. Micro-Raman Study of $\text{Ba}_{1-x}\text{Sr}_x\text{TiO}_3$ Ceramics. *J. Raman Spectrosc.* **2001**, *32*, 147–149.
- Menoret, C.; Kiat, J. M.; Dkhil, B.; Dammak, H.; Hernandez, O. Structural Evolution and Polar Order in $\text{Sr}_{1-x}\text{Ba}_x\text{TiO}_3$. *Phys. Rev. B* **2002**, *65*, 224104.
- Lemanov, V. V. Barium Titanate-Based Solutions. *Ferroelectrics* **2007**, *354*, 69–76.
- Hennings, D.; Schnell, A.; Simon, G. Diffuse Ferroelectric Phase Transitions in $\text{Ba}(\text{Ti}_{1-y}\text{Zr}_y)\text{O}_3$ Ceramics. *J. Am. Ceram. Soc.* **1987**, *65*, 539–544.
- Ravez, J.; Simon, A. Temperature and Frequency Dielectric Response of Ferroelectric Ceramics with Composition $\text{Ba}(\text{Ti}_{1-x}\text{Zr}_x)\text{O}_3$. *Eur. J. Solid State Inorg. Chem.* **1997**, *34*, 1199–1209.
- Dobal, P. S.; Dixit, A.; Katiyar, R. S.; Yu, Z.; Guo, R.; Bhalla, A. S. Micro-Raman Scattering and Dielectric Investigations of Phase Transition Behavior in the BaTiO_3 – BaZrO_3 System. *J. Appl. Phys.* **2001**, *89*, 8085–8091.
- Arlt, G.; Hennings, D.; de With, G. Dielectric Properties of Fine-Grained Barium Titanate Ceramics. *J. Appl. Phys.* **1985**, *58*, 1619–1625.
- Frey, M. H.; Payne, D. A. Grain-Size Effect on Structure and Phase Transitions for Barium Titanate. *Phys. Rev. B* **1996**, *54*, 3158–3168.
- Zhao, Z.; Buscaglia, V.; Viviani, M.; Buscaglia, M. T.; Mitoseriu, L.; Testino, A.; Nygren, M.; Johnsson, M.; Nanni, P. Grain-Size Effects on the Ferroelectric Behavior of Dense Nanocrystalline BaTiO_3 Ceramics. *Phys. Rev. B* **2004**, *70*, 024107.
- Petkov, V.; Buscaglia, V.; Buscaglia, M. T.; Zhao, Z.; Ren, Y. Structural Coherence and Ferroelectricity Decay in Sub-micron- and Nano-Sized Perovskites. *Phys. Rev. B* **2008**, *78*, 054107.
- Junquera, J.; Ghosez, P. Critical Thickness for Ferroelectricity in Perovskite Ultrathin Films. *Nature* **2003**, *422*, 506–509.
- Tenne, D. A.; Bruchhausen, A.; Lanzillotti-Kimura, N. D.; Fainstein, A.; Katiyar, R. S.; Cantarero, A.; Soukiasian, A.; Vaithyanathan, V.; Haeni, J. H.; Tian, W.; et al. Probing Nanoscale Ferroelectricity by Ultraviolet Raman Spectroscopy. *Science* **2006**, *323*, 1614–1616.
- Uchino, K.; Sadanaga, E.; Hirose, T. Dependence of the Crystal Structure on Particle Size in Barium Titanate. *J. Am. Ceram. Soc.* **1989**, *72*, 1555–1558.
- Frenkel, A. I.; Frey, M. H.; Payne, D. A. XAFS Analysis of Particle Size Effect on Local Structure in BaTiO_3 . *J. Synchrotron Rad.* **1999**, *6*, 515–517.
- Yashima, M.; Hoshina, T.; Ishimura, D.; Kobayashi, S.; Nakamura, W.; Tsurumi, T.; Wada, S. Size Effect on the Crystal Structure of Barium Titanate Nanoparticles. *J. Appl. Phys.* **2005**, *98*, 014313.
- Petkov, V.; Gateshki, M.; Niederberger, M.; Ren, Y. Atomic-Scale Structure of Nanocrystalline $\text{Ba}_x\text{Sr}_{1-x}\text{TiO}_3$ ($x = 1, 0.5, 0$) by X-ray Diffraction and the Atomic Pair Distribution Function Technique. *Chem. Mater.* **2006**, *18*, 814–821.
- Shiratori, Y.; Pithan, C.; Dornseiffer, J.; Waser, R. Raman Scattering Studies on Nanocrystalline BaTiO_3 : Part I—Isolated Particles and Aggregates. *J. Raman Spectrosc.* **2007**, *38*, 1288–1299.
- Smith, M. B.; Page, K.; Siegrist, T.; Redmond, P. L.; Walter, E. C.; Seshadri, R.; Brus, L. E.; Steigerwald, M. L. Crystal Structure and the Paraelectric-to-Ferroelectric Phase Transition of Nanoscale BaTiO_3 . *J. Am. Chem. Soc.* **2008**, *130*, 6955–6963.
- Szwarcman, D.; Lubk, A.; Linck, M.; Vogel, K.; Lereah, Y.; Lichte, H.; Markovich, G. Ferroelectric Effects in Individual BaTiO_3 Nanocrystals Investigated by Electron Holography. *Phys. Rev. B* **2012**, *85*, 134112.
- Polking, M. J.; Han, M.-G.; Yourdkhani, A.; Petkov, V.; Kisielowski, C. F.; Volkov, V. V.; Zhu, Y.; Caruntu, G.;

- Alivisatos, A. P.; Ramesh, R. Ferroelectric Order in Individual Nanometre-Scale Crystals. *Nat. Mater.* **2012**, *11*, 700–709.
27. Tiwari, V. S.; Singh, N.; Pandey, D. Diffuse Ferroelectric Transition and Relaxational Dipolar Freezing in (Ba,Sr)TiO₃. *J. Phys.: Condens. Matter* **1995**, *7*, 1441–1460.
28. Tenne, D. A.; Soukiassian, A.; Zhu, M. H.; Clark, A. M.; Xi, X. X.; Choosuwan, H.; He, Q.; Guo, R.; Bhalla, A. S. Raman Study of Ba_xSr_{1-x}TiO₃ Films: Evidence for the Existence of Polar Nanoregions. *Phys. Rev. B* **2003**, *67*, 012302.
29. Lauth, C.; Hippert, F.; Kreisel, J.; Maglione, M.; Simon, A.; Hazemann, J.-L.; Nassif, V. EXAFS Study of Lead-Free Relaxor Ferroelectric BaTi_{1-x}Zr_xO₃ at the Zr K Edge. *Phys. Rev. B* **2006**, *74*, 014106.
30. Karan, N. K.; Katiyar, R. S.; Maiti, T.; Guo, R.; Bhalla, A. S. Raman Spectral Studies of Zr⁴⁺-rich BaZr_xTi_{1-x}O₃ (0.5 < x < 1.00) Phase Diagram. *J. Raman Spectrosc.* **2008**, *40*, 370–375.
31. Akbarzadeh, A. R.; Prosandeev, S.; Walter, E. J.; Al-Barakaty, A.; Bellaiche, L. Finite-Temperature Properties of Ba(Zr,Ti)O₃ Relaxors From First Principles. *Phys. Rev. Lett.* **2012**, *108*, 257601.
32. Osada, M.; Sasaki, T. Two-Dimensional Dielectric Nanoheats: Novel Nanoelectronics From Nanocrystal Building Blocks. *Adv. Mater.* **2012**, *24*, 210–228.
33. Aygun, S. M.; Ihlefeld, J. F.; Borland, W. J.; Maria, J.-P. Permittivity Scaling in Ba_{1-x}Sr_xTiO₃ Thin Films and Ceramics. *J. Appl. Phys.* **2011**, *109*, 034108.
34. Beier, C. W.; Cuevas, M. A.; Brutchey, R. L. Low-Temperature Synthesis of Solid-Solution Ba_xSr_{1-x}TiO₃ Nanocrystals. *J. Mater. Chem.* **2010**, *20*, 5074–5079.
35. Rabuffetti, F. A.; Brutchey, R. L. Local Structural Distortion of BaZr_xTi_{1-x}O₃ Nanocrystals Synthesized at Room Temperature. *Chem. Commun.* **2012**, *48*, 1437–1439.
36. Rabuffetti, F. A.; Lee, J. S.; Brutchey, R. L. Low Temperature Synthesis of Complex Ba_{1-x}Sr_xTi_{1-y}Zr_yO₃ Perovskite Nanocrystals. *Chem. Mater.* **2012**, *24*, 3114–3116.
37. Kraizman, V. L.; Novakovich, A. A.; Vedrinskii, R. V.; Timoshevskii, V. A. Formation of the Pre-Edge Structure and Dramatic Polarization Dependence of Ti K NEXAFS in PbTiO₃ Crystals. *Phys. B* **1995**, *209*, 35–36.
38. Ravel, B. Ferroelectric Phase Transitions in Oxide Perovskites Studied by XAFS. Ph.D. Thesis, University of Washington, 1997.
39. Ravel, B.; Stern, E. A.; Vedrinskii, R. I.; Kraizman, V. Local Structure and the Phase Transitions of BaTiO₃. *Ferroelectrics* **1998**, *206*, 407–430.
40. Vedrinskii, R. V.; Kraizman, V. L.; Novakovich, A. A.; Demekhin, P. V.; Urazhdin, S. V. Pre-Edge Fine Structure of the 3d Atom K X-ray Absorption Spectra and Quantitative Atomic Structure Determinations for Ferroelectric Perovskite Structure Crystals. *J. Phys.: Condens. Matter* **1998**, *10*, 9561–9580.
41. Levin, I.; Kraizman, V.; Woicik, J. C. Local-Structure Origins of the Sustained Curie Temperature in (Ba,Ca)TiO₃ Ferroelectrics. *Appl. Phys. Lett.* **2013**, *102*, 162906.
42. Levin, I.; Cockayne, E.; Kraizman, V.; Woicik, J. C.; Lee, S.; Randall, C. A. Local Structure of Ba(Ti,Zr)O₃ Perovskite-Like Solid Solutions and its Relation to the Band-Gap Behavior. *Phys. Rev. B* **2011**, *83*, 094122.
43. Shuvaeva, V.; Azuma, Y.; Yagi, K.; Terauchi, H.; Vedrinskii, R.; Komarov, V.; Katsani, H. Ti Off-Center Displacements in Ba_{1-x}Sr_xTiO₃ Studied by EXAFS. *Phys. Rev. B* **2000**, *62*, 2969–2972.
44. Rabuffetti, F. A.; Brutchey, R. L. Structural Evolution of BaTiO₃ Nanocrystals Synthesized at Room Temperature. *J. Am. Chem. Soc.* **2012**, *134*, 9475–9487.
45. Egami, T.; Billinge, S. J. L. *Underneath The Bragg Peaks: Structural Analysis of Complex Materials*; Pergamon: Oxford, UK, 2003.
46. Pasciak, M.; Welberry, R. Diffuse Scattering and Local Structure Modeling in Ferroelectrics. *Z. Kristallogr.* **2011**, *226*, 113–1125.
47. Dec, S. F.; Davis, M. F.; Maciel, G. E.; Bronnimann, C. E. Solid-State Multinuclear NMR Studies of Ferroelectric, Piezoelectric, and Related Materials. *Inorg. Chem.* **1993**, *32*, 955–959.
48. Haskel, D.; Ravel, B.; Newville, M.; Stern, E. A. Single and Multiple Scattering XAFS in BaZrO₃: A Comparison between Theory and Experiment. *Phys. B* **1995**, *208*–209, 151–153.
49. Petzelt, J.; Ostapchuk, T.; Gregora, I.; Rychetsky, I.; Hoffman-Eifert, S.; Pronin, A. V.; Yuzyuk, Y.; Gorshunov, B. P.; Kamba, S.; Bovtun, V.; et al. Dielectric, Infrared, and Raman Response of Undoped SrTiO₃ Ceramics: Evidence of Polar Grain Boundaries. *Phys. Rev. B* **2001**, *64*, 184111.
50. Sirenko, A. A.; Akimov, I. A.; Fox, J. R.; Clark, A. M.; Li, H. C.; Si, W.; Xi, X. X. Observation of the First-Order Raman Scattering in SrTiO₃ Thin Films. *Phys. Rev. Lett.* **1999**, *82*, 4500–4503.
51. Rabuffetti, F. A.; Kim, H.-S.; Enterkin, J. A.; Wang, Y.; Lanier, C. H.; Stair, P. C.; Marks, L. D.; Poeppelmeier, K. R. Synthesis-Dependent First-Order Raman Scattering in SrTiO₃ Nanocubes at Room Temperature. *Chem. Mater.* **2008**, *20*, 5628–5635.
52. Junquera, J.; Ghosez, P. Critical Thickness for Ferroelectricity in Perovskite Ultrathin Films. *Nature* **2003**, *422*, 506–509.
53. Jeong, I.-K.; Park, C. Y.; Ahn, J. S.; Park, S.; Kim, D. J. Ferroelectric-Relaxor Crossover in Ba(Ti_{1-x}Zr_x)O₃ Studied Using Neutron Total Scattering Measurements and Reverse Monte Carlo Modeling. *Phys. Rev. B* **2010**, *81*, 214119.
54. Joseph, J.; Vimala, T. M.; Raju, J.; Murthy, V. R. K. Structural Investigations on the (Ba,Sr)(Zr,Ti)O₃ System. *J. Phys. D: Appl. Phys.* **1999**, *32*, 1049–1057.
55. Kreisel, J.; Bouvier, P.; Maglione, M.; Dkhil, B.; Simon, A. High-Pressure Raman Investigation of the Pb-Free Relaxor BaTi_{0.65}Zr_{0.35}O₃. *Phys. Rev. B* **2004**, *69*, 092104.
56. Ravel, B.; Newville, M. *J. Synchrotron Rad.* **2005**, *12*, 537–541.
57. Larson, A. C.; Von Dreele, R. B. *General Structure Analysis System (GSAS)*; Los Alamos National Laboratory: New Mexico, 2000.
58. Thomson, P.; Cox, D. E.; Hasting, J. M. Rietveld Refinement of Debye-Scherrer Synchrotron X-Ray data from Al₂O₃. *J. Appl. Crystallogr.* **1987**, *20*, 79–83.
59. Young, R. A. *The Rietveld Method*; Oxford University Press: New York, 1993.
60. Petkov, V. RAD, A Program for Analysis of X-ray Diffraction Data from Amorphous Materials for Personal Computers. *J. Appl. Crystallogr.* **1989**, *22*, 387–389.
61. Farrow, C. L.; Juhas, P.; Liu, J. W.; Bryndin, D.; Bozin, E. S.; Bloch, J.; Proffen, T.; Billinge, S. J. L. PDFfit2 and PDFgui: Computer Programs for Studying Nanostructure in Crystals. *J. Phys.: Condens. Matter* **2007**, *19*, 335219.
62. Petkov, V. *Characterization of Materials*; John Wiley & Sons, Inc.: New York, 2012.